iScience

CellPress
OPEN ACCESS

Article

Highly porous and rough polydimethylsiloxane film-based triboelectric nanogenerators and its application for electrochemical cathodic protection

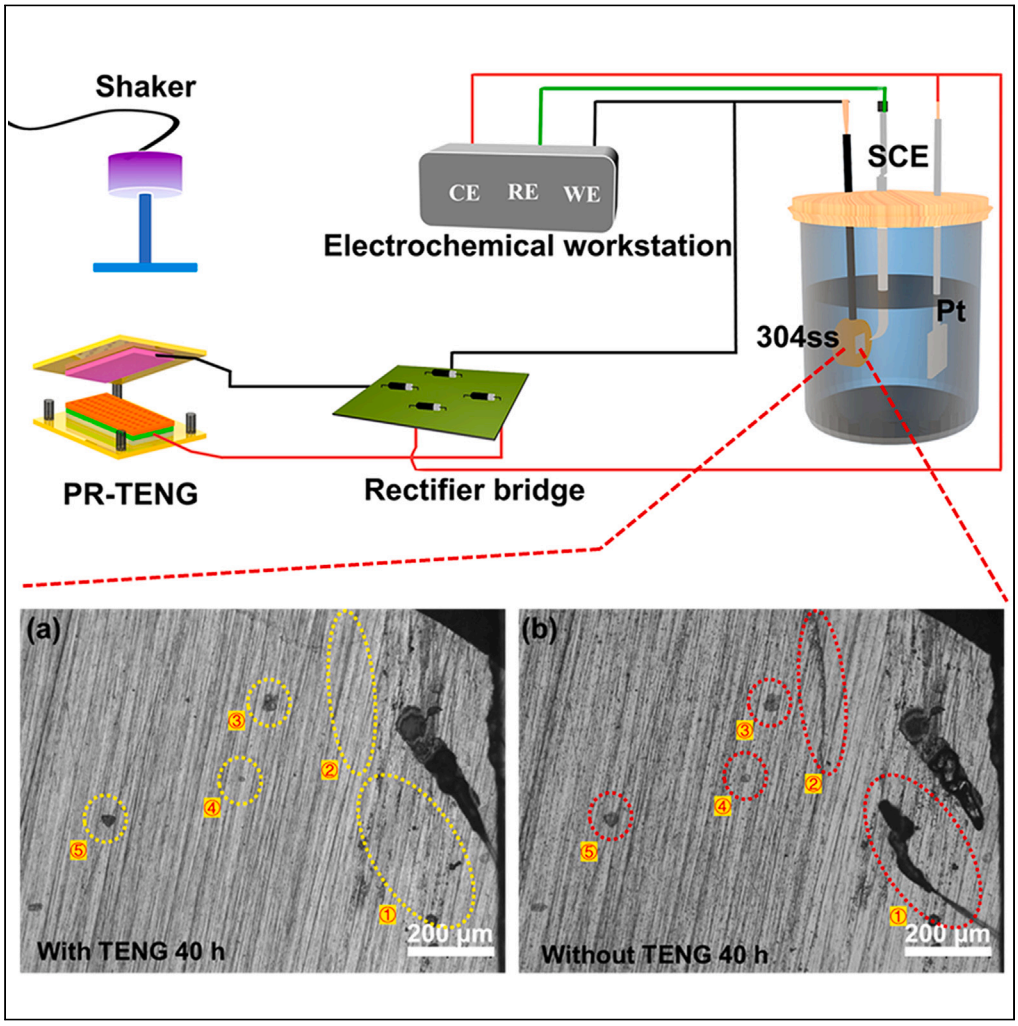

Youbo Nan, Xiutong Wang, Hui Zhou, Yanan Sun, Teng Yu, Lihui Yang, Yanliang Huang

wangxiutong@qdio.ac.cn

Highlights

A porous and high-roughness PDMS (PR/PDMS) negative friction layer was prepared

Based on the PR/PDMS, a triboelectric nanogenerator (PR-TENG) was fabricated

PR-TENG has excellent electrical performance with good stability and huge output

PR-TENG works as a clean energy source for electrochemical processes

Nan et al., iScience 26, 108261
November 17, 2023
https://doi.org/10.1016/j.isci.2023.108261

iScience

CellPress
OPEN ACCESS

Article

Highly porous and rough polydimethylsiloxane film-based triboelectric nanogenerators and its application for electrochemical cathodic protection

Youbo Nan,[1,3] Xiutong Wang,[1,2,3,4,5,*] Hui Zhou,[1] Yanan Sun,[1] Teng Yu,[1] Lihui Yang,[1] and Yanliang Huang[1]

SUMMARY

The development and utilization of triboelectric nanogenerator (TENG) are very important for realizing energy cleaning in electrochemical processes. However, limited electrical output performance plays a major stumbling block to this process. Herein, a porous and high-roughness PDMS (PR/PDMS) negative friction layer was obtained by doping PDMS with powdered chitosan and casting using a sacrificial anodic alumina template. A TENG was fabricated by the PR/PDMS with Al film (PR-TENG). The PR-TENG exhibited much better performance than the pure PDMS-based TENG, which was attributed to the porous properties of the PR/PDMS. Under the driving of external mechanical force at 5 Hz, the PR-TENG showed a maximum output open-circuit voltage (V_{oc}) and short-circuit current density (J_{sc}) of 77.1 V and 33.9 mA/m^2, respectively. To prove the concept, the electrochemical cathodic protection system with PR-TENG was constructed. Ultimately, the application prospects of the PR-TENG as a clean energy source for electrochemical processes were explored and evaluated.

INTRODUCTION

The development of low-carbon, clean, and sustainable energy is gaining momentum because of energy shortage and environmental problems.[1–3] Currently, a considerable amount of electrical energy is consumed in electrochemical processes; therefore, the development and utilization of clean and sustainable energy for electrochemical processes have attracted extensive attention in recent years.[4] In 2012, Wang et al.[5,6] invented triboelectric nanogenerators (TENGs), the use of which is a promising route for supplying clean energy to the electrochemical processes.[7–14] TENG has the following advantages: a wide selection of materials, light weight, low cost, and easy capturing low-frequency mechanical oscillations.[15–17] However, TENGs also possess the disadvantages of low electrical output, high matching impedance, and poor stability.[14,15,18] In which the low electrical output is a critical drawback limiting the practical application of TENGs. However, TENG output may be enhanced through material selection and modification.[19–22] Polydimethylsiloxane (PDMS) is widely used in the construction of TENGs because of its non-toxicity, good flexibility, transparency, good biocompatibility, simple preparation, and low cost.[23–26] More importantly, PDMS is easily modified both on the surface or in bulk, which is conducive to achieving high performance.[27–33] Surface engineering is an important strategy for improving electrical output performance of TENG. This strategy mainly includes the improvement of the surface geometry and surface modification of the friction layer. The geometric morphology improvement is mainly through chemical etching, plasma treatment, laser treatment, and electrostatic spinning techniques to create a rough surface with micro/nano structure.[34–37] Surface roughness is an important factor affecting the TENGs output: it increases with the increasing surface roughness.[38–40] Wang et al.[41] designed the pyramid and cubic patterns PDMS to improve the output of TENG. Huang et al.[42] obtained micro-nano structures on the friction layer using laser scanning technology to enhance the output of the TENG, which greatly promotes the practicality of the TENG in large-scale manufacturing and micro-energy utilization. In addition, surface modification is an important way to improve TENG performance. Wang et al. improved the performance of TENG by using self-assembled monolayer (SAMs) to functionalize the surface. Li et al.[43] regulated the chemical structure and functional groups of the triboelectric polymer at the molecular level by means of low-energy ion irradiation, which opened up a new breakthrough in the field of triboelectric materials. Moreover, a high ratio of surface area to volume can not only reduce the effective thickness of the friction material but also regulate its dielectric constant, which is helpful for improving the output performance of TENGs.[12,44] Some researchers have focused on achieving ratio of surface area to volume by designing friction layers with a porous structure. Sacrificial template method is an important method to prepare porous structure friction. Fan et al.[45] prepared stretchable TENG with NaCl template, whose open-circuit voltage and short-circuit current were 60V and 180 nA, respectively. Cui et al.[46] prepared friction layer based on

[1]Key Laboratory of Marine Environmental Corrosion and Bio-fouling, Institute of Oceanology, Chinese Academy of Sciences, Qingdao 266071, China
[2]Open Studio for Marine Corrosion and Protection, Laoshan Laboratory, Qingdao 266237, China
[3]University of Chinese Academy of Sciences, Beijing 100049, China
[4]Center for Ocean Mega-Science, Chinese Academy of Sciences, Qingdao 266071, China
[5]Lead contact
*Correspondence: wangxiutong@qdio.ac.cn
https://doi.org/10.1016/j.isci.2023.108261

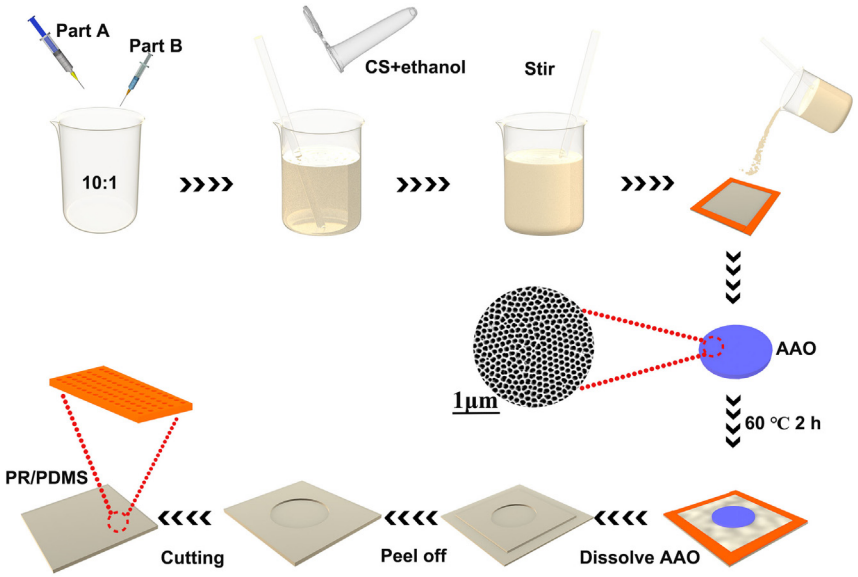

Figure 1. Schematic of the preparation of the PR/PDMS

porous Na_2CO_3/PDMS to improve the output performance of TENG, which realized the collection and conversion of mechanical energy for human movement. Although some porous friction layers have been reported. However, more porous friction layers and preparation methods conducive to the performance improvement of TENG should still be explored. Moreover, techniques simultaneously increasing the surface roughness and the ratio of PDMS surface area to volume need to be explored to enhance the TENG output.

In this work, a porous and high-roughness PDMS (PR/PDMS) negative friction layer was obtained by doping PDMS with powdered chitosan and casting using a sacrificial anodic aluminum oxide (AAO) template. The PR/PDMS negative friction layer was fabricated for constructing a TENG with Al as the positive layer (PR-TENG). Under the driving of external mechanical force at 5 Hz, PR-TENG exhibited the maximum *Voc* and J_{sc} output of 77.1 V and 33.9 mA/m^2, respectively. In addition, the PR-TENG under 5 Hz mechanical energy was capable of driving 450 commercial LED lamps, indicating that the PR-TENG can provide electric energy as an energy conversion device. In addition, the electrochemical cathodic protection system powered by the PR-TENG was constructed. The results showed that TENG provided stable cathodic protection for 304 stainless steel (304ss) under 1–5 Hz mechanical force. In which, the open circuit potential (OCP) on the 304ss was reduced below the self-corrosion potential thereof. Ultimately, the results showed that the PR-TENG is a promising clean energy source for electrochemical processes.

RESULTS AND DISCUSSION

Fabrication and characterization of porous and high-roughness/polydimethylsiloxane

Figure 1 shows a schematic of the fabrication of PR/PDMS. The PR/PDMS was obtained by doping powdered chitosan and sacrificial AAO template. First of all, the chitosan ethanol suspension was added into PDMS to form a thorough mixing. The mixture was poured into a mold prepared from an acrylic sheet and Kapton tape. The AAO template was placed on the mixture and left to stand by. The PR/PDMS was obtained after the heat curing and etching of the AAO template with NaOH solution (detailed information will be described in the Experimental Section).

To explore the effects of porous structure and surface roughness of the friction material on the electrical output performance of TENG, the microstructure of the PR/PDMS was characterized by laser scanning confocal microscopy (LSCM) and scanning electron microscopy (SEM). In addition, the pure PDMS and chitosan-doped PDMS (CS/PDMS) were prepared for comparison. The XRD patterns of the PDMS and CS/PDMS are shown in Figure S1. The peaks at 2θ values of 12° and 22° are attributed to the PDMS. The decrease trend of 2θ values of 12° and 22° in CS/PDMS was attributed to the effect of CS interference on the crystallization of PDMS.[47,48] In addition, no obvious characteristic peaks of CS were observed, which may be due to the small amount of CS doping. FTIR was used to analyze the chemical groups on the surface of samples (Figure S2). The peaks observed in the PDMS curve at 2962, 1259, 1014 and 798 cm^{-1} were attributed to the $-CH_3$ group, Si−CH3, Si-*O*-Si, and C-Si-C, respectively.[47,49] No other obvious characteristic peaks were found in the CS/PDMS curve, which indicated that CS and PDMS were only physical miscible without chemical interaction.[49] Optical photographs show that the surface of the pure PDMS is smooth and free of impurities and that the PDMS has very good transparency (Figure S3A). The CS/PDMS and PR/PDMS have rough surfaces, and both samples exhibit a significantly lower transparency (Figures S3B and S3C)), which was attributed to chitosan doping. Simultaneously, the 3D morphologies of the CS/PDMS and PR/PDMS show a large number of small bumps on the surface, compared with the pure PDMS (Figures 2A–2C). SEM further confirms the roughness of the CS/PDMS and PR/PDMS surfaces, as shown in Figures 2D–2F. In addition,

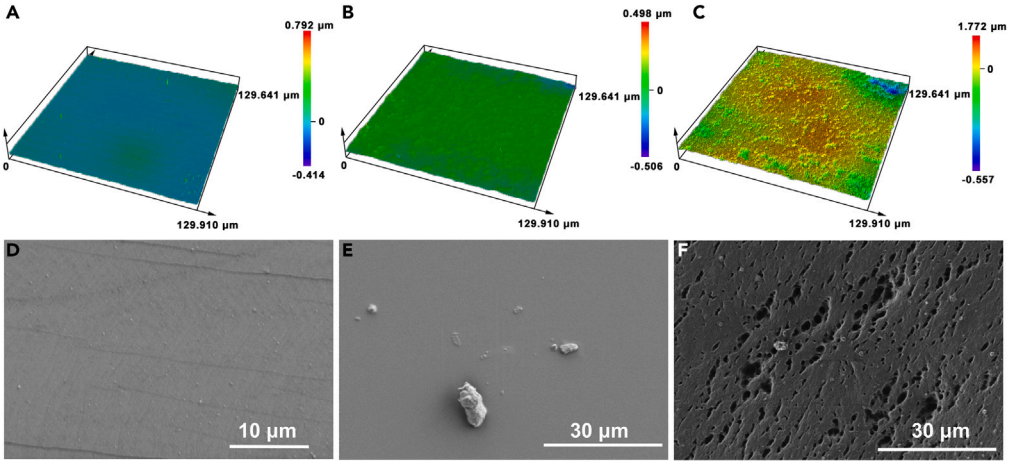

Figure 2. The 3D morphologies and SEM images of the pure PDMS, CS/PDMS, and PR/PDMS

LSCM 3D morphologies of (A) pure PDMS, (B) CS/PDMS, and (C) PR/PDMS. SEM images of (D) pure PDMS, (E) CS/PDMS, and (F) PR/PDMS.

Figures S4A–S4C show the cross-section SEM images of PDMS, CS/PDMS, and PR/PDMS. The results show that the thickness of the three friction materials is about 520 ± 10 μm. Meanwhile, the cross-section of PR/PDMS exposes a large number of irregular pore structures and air sacs. A magnified image of the hole and corresponding elements mappings are obtained from Figure S4C, as shown in Figures S4D and S4E). The results show that PR/PDMS also have a porous structure.

The roughness of the PR/PDMS surface was attributed to its porous structure, which is formed owing to chitosan doping and AAO template treatment. Related studies have reported that rough and porous structures can not only effectively reduce the thickness of the friction layer and increase the contact surface, but also lead to a large number of micro-capacitors for increasing the surface charge density (σ) of the friction layer,[50–52] ultimately improving the electrical output of TENGs. An arithmetic mean height (Sa) and root-mean-square height (Sq) of the PR/PDMS surface are 0.533 μm and 0.723 μm, respectively, which are significantly higher than those of the pure PDMS and CS/PDMS (Figure 3).

Structural, mechanism, and output characterization of the porous and high-roughness-triboelectric nanogenerator

Figure 4A shows a schematic of a PR-TENG sandwich-like architecture. The negative and positive friction materials are PR/PDMS and Al foil, respectively. The PR-TENG operates in a contact-separated mode and is driven by an external mechanical force, as shown in Figure 4B.

The mechanism of the TENG is based on the coupling of the triboelectric effect and electrostatic induction. Figure 5 illustrates the working mechanism of the PR-TENG, showing that electricity is generated through four processes. In the initial state, as shown in Figure 5A, the PR/PDMS

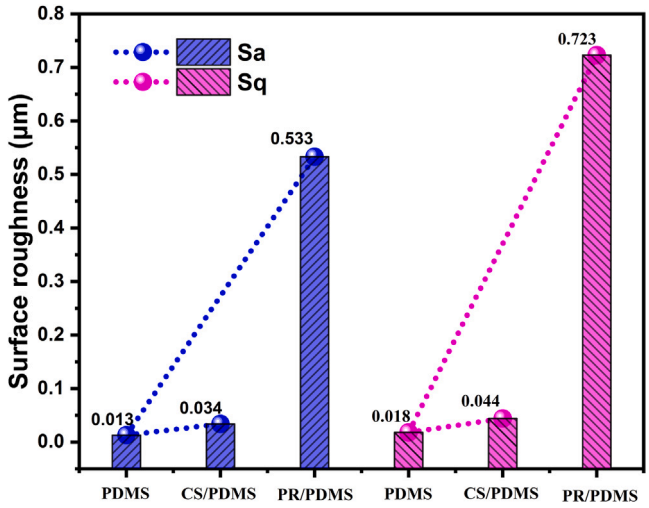

Figure 3. Surface roughness of the pure PDMS, CS/PDMS, and PR/PDMS

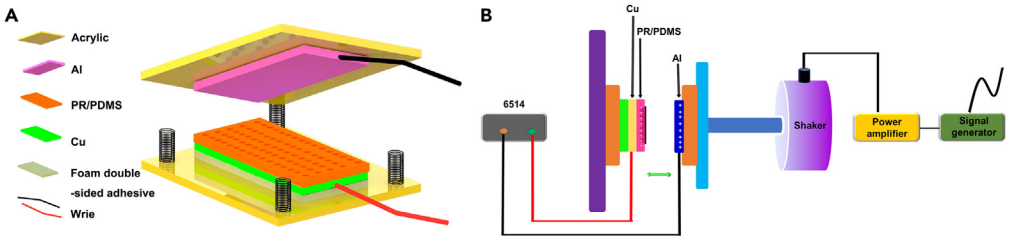

Figure 4. Schematic of the PR-TENG and the driving device

(A) Schematic of the PR-TENG sandwich-like architecture.

(B) Schematic of the driving device for PR-TENG performance evaluation.

and the Al foil are separated and are both in an electrically neutral state. When they are pressed into each other, equal and opposite charges are gained: the PR/PDMS becomes negatively charged, and the Al foil becomes positively charged (Figure 5B). When the external mechanical force is removed, the PR/PDMS and the Al foil begin to be separated. At this time, because the potential of the Al foil is higher than that of the copper electrode on the backside of the PR/PDMS, the current flows into the copper electrode on the backside of the PR/PDMS along the external circuit (Figure 5C). As a result, at the moment when the PR/PDMS is completely separated from the Al foil, the charges of the Al foil has been completely lost, while the copper electrode on the backside of the PR/PDMS has gained equal positive charges (Figure 5D). When the PR/PDMS and Al foil are brought closer together again, an opposite current starts to flow (Figure 5E). Thus, under the action of external mechanical force, the reciprocating contact and separation induce a pulsed alternating current.

To explore the electrical output performance of PR-TENG, the open-circuit voltage (V_{oc}) and short-circuit current density (J_{sc}) were measured at a driving frequency of 5 Hz. The maximum peak V_{oc} values for the TENGs based on the pure PDMS and CS/PDMS are 42.5 and 50.4 V, respectively. The maximum peak V_{oc} value for the PR-TENG is 77.1 V, as shown in Figure 6A. The TENG based on the pure PDMS and CS/PDMS exhibit the maximum J_{sc} peak values of 15.2 and 14.5 mA/m^2, respectively. The maximum J_{sc} peak value for the PR-TENG is 33.9 mA/m^2, as shown in Figure 6B. Compared with the TENG based on the pure PDMS, the CS/PDMS-based TENG and PR-TENG show significantly higher V_{oc}. Although the J_{sc} of the CS/PDMS-based TENG is not significantly higher than that of pure PDMS-based TENG, that of the PR-TENG is considerably higher than that of pure PDMS-based TENG. The V_{oc} and J_{sc} of CS/PDMS-based TENG were not significantly higher than those of pure PDMS-based TENG, or even slightly lower, which was attributed to the multiple functional groups of chitosan. Furthermore, the transferred charges are calculated using the following equation:

$$Q = \int I dt$$

where I is the values of short-circuit current. Compared with TENG based on pure PDMS, the CS/PDMS-based TENG and PR-TENG show significantly higher contacted charges (Qc) and separated charges (Qs), as shown in Figures 6C–6E. In addition, Qc and Qs are almost equal,

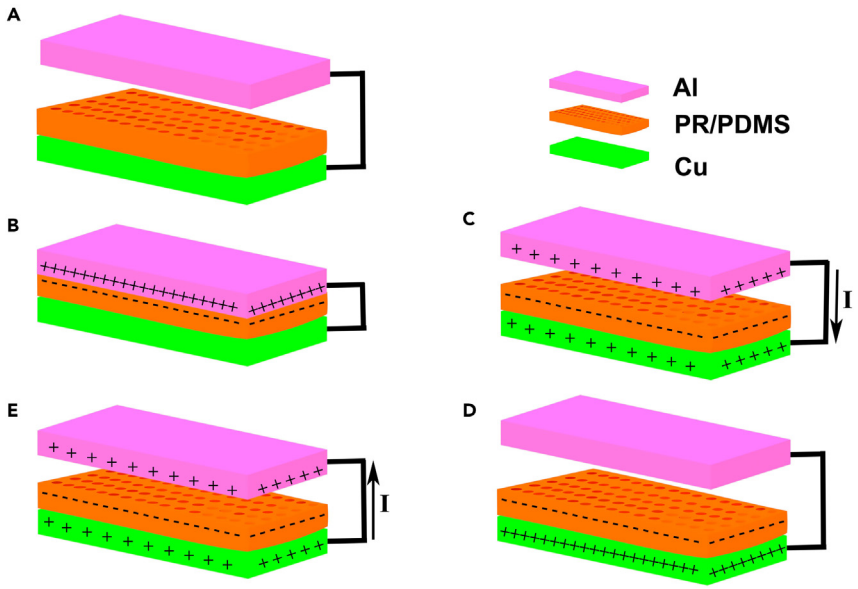

Figure 5. Schematic of working mechanism of the PR-TENG

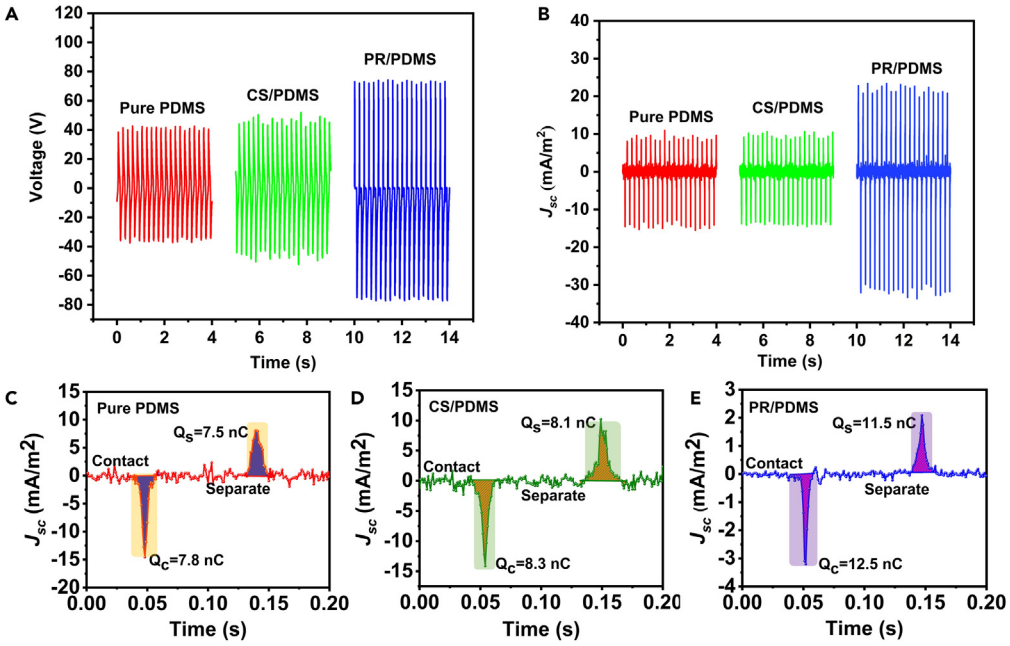

Figure 6. Output performance curve of the TENGs

(A) output voltage (V_{oc}); (B) short-circuit current density (J_{sc}); (C–E) transferred charges.

while the peak value of contact current is greater than the peak value of separation current, which is attributed to the slower separation process of TENG because the process is driven by the restorative force of the spring.[53]

It is worth noting that the electrical performance of PR-TENG was significantly improved over the control samples, which was mainly attributed to the effect of the porous and high-roughness surface of PR/PDMS. Related literature reports that the main factor affecting the electrical output performance of TENGs is the surface charge density (σ),[54–56] and the roughness of the electrode surface can greatly affect σ. The friction layer with high roughness can effectively enhance the contact area and thus improve the output performance of TENG.[38,57] In addition, the working distance between the friction layers (1–2 mm) and the thickness of the friction layer (0.18 mm) of the TENG in this work are rather small compared to the friction surface (15 × 15 mm). Therefore, TENG is equivalent to multiple parallel plate capacitors (Figure S5A), such that

$$C = \frac{\varepsilon A}{d} \quad \text{(Equation 1)}$$

where C is the capacitance, ε is the dielectric constant of the friction layer, A is the area of the friction layer, and d is the thickness of the friction layer. The magnitude of C mainly depends on the size of d. As d decreases, C increases. Herein, the air in the PR/PDMS pores is equivalent to a thin air layer of thickness x_i. Therefore, the total thickness of the air layer is $\delta = \sum_i x_i$. The thickness of the porous PR/PDMS is greatly reduced by the external pressure owing to the discharge of the thin air layer, as shown in Figure S5B.

Thus, the capacitance (C_δ) of PR/PDMS under external pressure can be expressed as follows:

$$C_\delta = \frac{\varepsilon A}{d - \delta} \quad \text{(Equation 2)}$$

Equation 2 shows that C_δ increases significantly, meaning that the electrical output performance of PR-TENG increases as well. In addition, the discharge of a thin air layer increases the effective permittivity of PR/PDMS because the permittivity of air is lower than that of PDMS (ε_{air} = 1.0, ε_{PDMS} = 2.83).[7] Moreover, the addition of CS into PDMS is beneficial to improve its dielectric constant. As shown Figure S6A, the dielectric constant of SC/PDMS is higher than that of pure PDMS, which is beneficial to enhance the electrical output performance of TENG. The dielectric loss for both pure PDMS and SC/PDMS remained at low levels, as shown Figure S6B. In addition, for PDMS and CS/PDMS, the conductivity of the composite dielectric layer exhibits insulation performance at low frequencies, as shown in Figure S6C. This further increases the PR/PDMS capacitance, enhancing the electrical of the TENG. In addition, a friction layer with different sizes pore was prepared, as shown in Figures S7A–S7C. The pore sizes of PR/PDMS-0.54 and PR/PDMS-1.7 friction layers are 0.54 μm and 1.7 μm, respectively. Figures S7D–S7F shows the electrical output performance of TENGs based on pure PDMS, PR/PDms-0.54 and PR/PDms-1.7. The result shows the TENG output increases with increasing hole size. This is consistent with the theoretical predictions above.

The TENGs harvest the disordered low-frequency mechanical energy from the surrounding environment and convert it into usable electrical energy, which is significant for the development of clean and sustainable energy. The TENG performance was evaluated by exploring the relationship between TENG output performance and excitation frequency. Figures 7A and 7B show the V_{oc} and J_{sc} of the PR-TENG

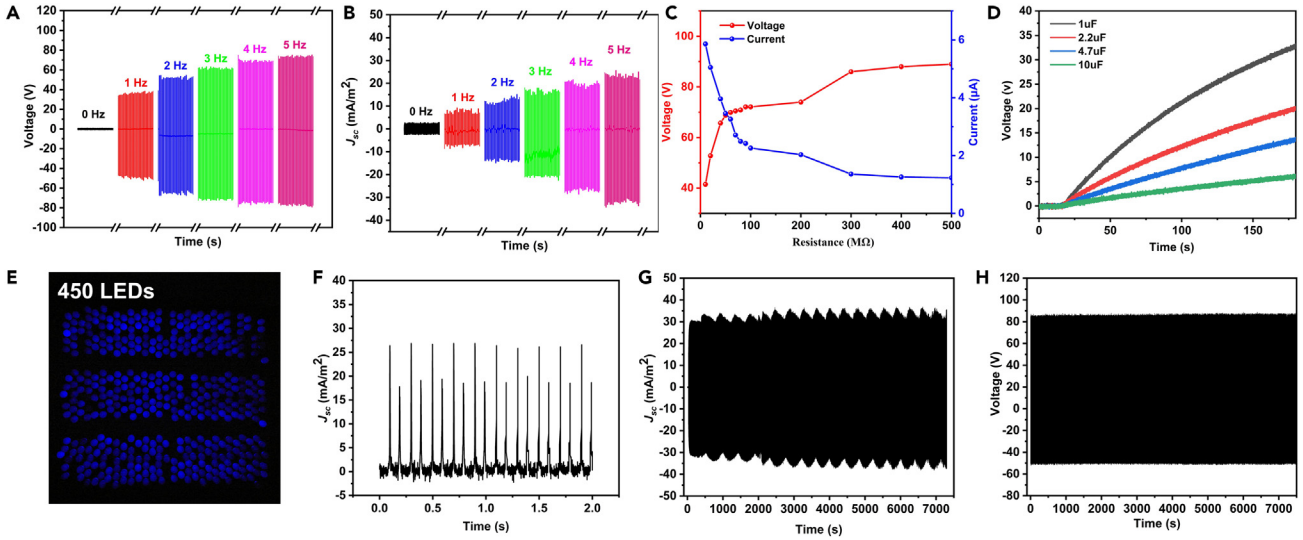

Figure 7. Output performance of the PR-TENG and applications

(A) V_{oc} and (B) J_{sc} of the PR-TENG at different frequencies.

(C) Maximum output voltage and current of the PR-TENG with different load resistances.

(D) Charging curve of capacitors.

(E) Photographs of 450 LEDs powered by the PR- TENG.

(F) Current output curve of PR-TENG after rectification.

(G) J_{sc} and (H) V_{oc} curves of PR-TENG within 37500 cycles.

operated at 0–5 Hz. The results show that the V_{oc} and J_{sc} increase with working frequency, which was attributed to an increase in the charge transfer rate with increasing speed of the reciprocating contact and separation. Moreover, the output performance of PR-TENG dependence on the external forces, as shown in Figure S8. The results show that V_{oc} and J_{sc} increase with external forces, which was attributed to increase in the deformation of PR/PDMS and the contact area between Al. It is worth mentioning that the electrical output performance of the PR-TENG is comparable to or superior to that of many previous porous TENG devices (Table 1).

The PR-TENG output performance is affected by the load. Figure 7C shows the maximum output voltage and current exhibited by PR-TENG at different load resistances. The results show that the output voltage and current of PR-TENG increase and decrease, respectively, with the increase in load. In addition, the maximum output power density is 118.5 mW/m^2 at a load of 20 MΩ (Figure S9). In the light of the excellent electrical output capability, the PR-TENG was used to charge capacitors with capacities of 1, 2.2, 4.7, and 10 μF. The charging curves in Figure 7D show that capacitors were charged quickly and consistently, indicating that the PR-TENG is promising for converting mechanical energy and storing electrical energy. Furthermore, to verify the application of PR-TENG as a power conversion device, it was tested to power LED lights. As shown in Figure 7E and Video S1, PR-TENG could drive 450 commercial LED lamps under the action of 5 Hz mechanical energy. The corresponding rectified current curve and circuit diagram are shown in Figures 7F and S10, respectively. Energy converters must be able to provide a stable power supply for a long time. Therefore, the stability of the PR-TENG output was tested. Figure 7G and Figure 7 show the J_{sc} and V_{oc} curves for 37500 cycles under the driving frequency of 5 Hz. The results show that both the voltage output signal and the

Table 1. Comparison of some relevant works reported for triboelectric nanogenerators based on the porous friction layer

TENGs	Force (N)	Frequency (Hz)	Voltage (V)	Current (μA)	Dimension (cm^2)
This work	40 N	5 Hz	80 V	9.8 μA	2.25 cm^2
Porous PDMS-nickel ferrite TENGs[58](2023)	/	/	60 V	0.3μA	/
PC-TENG[59](2022)	/	5 Hz	120 V	8 μA	4 cm^2
DS-TENG[60](2022)	30 N	4 Hz	50 V	0.5μA	9 cm^2
Porous PDMS TENGs[27](2021)	600 N	1 Hz	72 V	10 μA	/
Cu@PPy sponges-TENGs[61](2019)	/	1 Hz	45 V	0.4μA	2.25 cm^2
Flexible porous TENG[62] (2019)	42 N	/	91 V	2.87 μA	4 cm^2
A- NGs[52](2018)	/	/	60.6 V	7.7μA	2 cm^2
Stretchable TENG[45](2017)	60 N	/	60 V	0.18μA	6.25 cm^2

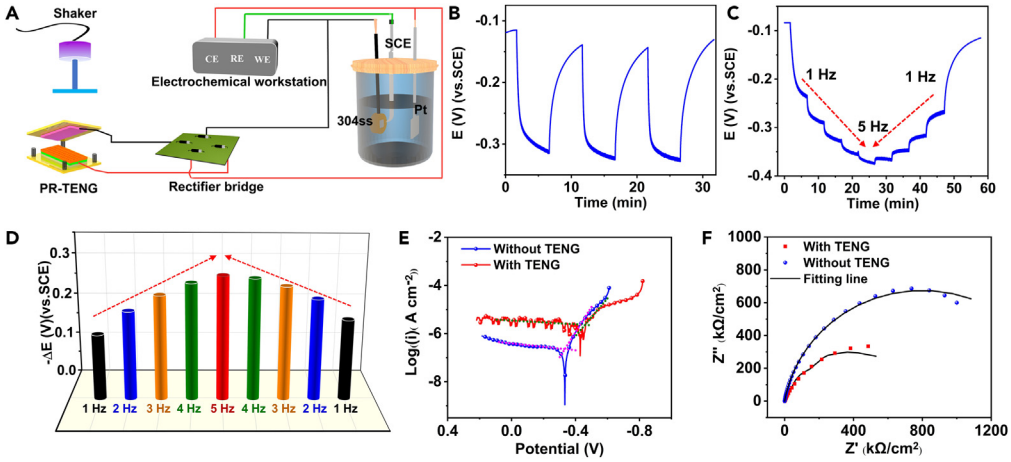

Figure 8. PR-TENG for cathodic protection

(A) Schematic of the device for the PR-TENG cathodic protection of 304ss.

(B) OCP of 304ss powered by PR-TENG at a driving frequency of 3Hz.

(C) OCP of 304ss powered by PR-TENG at driving frequencies.

(D) The potential drop on 304ss powered by PR-TENG at different driving frequencies.

(E) Polarization curves of 304ss with and without the PR-TENG.

(F) Nyquist curves of 304ss with and without the PR-TENG.

current signal of the PR-TENG remain stable after 37500 cycles. This indicates that the PR-TENG exhibits stable performance and has good application potential.

Application of porous and high-roughness-triboelectric nanogenerator for electrochemistry cathodic protection

To further demonstrate the application of the PR-TENG as a power conversion device, a cathodic protection system based on PR-TENG was constructed, as shown in Figure 8A. The cathodic protection parameters (OCP and polarization curve) of the assembled system for 304ss were tested, and the electrochemical impedance spectroscopy (EIS) was performed. As shown in Figure 8B and Video S2, the OCP of 304ss dropped to −330 mV when the PR-TENG was driven by a 3 Hz mechanical force, which is significantly lower than the self-corrosion potential, indicating successful cathodic protection. In addition, the OCP and current of 304ss protected by the PR-TENG at 1–5 Hz mechanical frequency were investigated, as shown in Figures 8C and S11. The results show that the OCP of 304ss is inversely related to the driving frequency. The current of cathodic protection 304ss increases with the increase in the driving frequency and decreases with the decrease in the driving frequency. The surface potential drop of 304ss is also directly related to the driving frequency, as shown in Figure 8D. In addition, the polarization curves and electrochemical parameters show a significant negative shift in the corrosion potential of 304ss of PR-TENG, which also indicates that PR-TENG can form cathodic protection for 304ss (Figure 8E and Table 2). Furthermore, the cathodic protection performance provided by PR-TENG was evaluated by EIS, as shown in Figures 8F and S12. The results show that the impedance of 304ss with PR-TENG cathodic protection is significantly lower than that of 304ss without PR-TENG. Figure S13 shows the EIS equivalent circuit, and Table 3 lists EIS parameters for 304ss with and without the PR-TENG. In Figure S13, R_s is the solution resistance, Q_{dl} is the double-layer capacitance, and R_{ct} is the charge-transfer resistance. The smaller the R_{ct}, the faster the charge transfer in the cathodic process on the 304ss surface, and the higher is the current in the circuit. Figures 9A and 9B display the optical images of 304ss with and without the PR-TENG after 40 h in 3.5 wt % NaCl solution. In contrast to the 304ss surface with TENG, the 304ss without TENG shows pitting corrosion. The above results show that PR-TENG can be used as a power conversion device for powering electrochemical cathodic protection.

Conclusions

The PR/PDMS negative friction layer was obtained by doping powdered chitosan and sacrificial AAO template. The results showed that the porous and rough friction layer enhanced the electrical performance of the TENG. The rough surface increased the contact area and

Table 2. Electrochemical parameters obtained from the Tafel curves of 304ss in 3.5 wt % NaCl solution with and without the PR-TENG

	E_{corr} (V(vs.SCE)	I_{corr}(μA)	$-\beta_c$ (mV dec^{-1})	β_a (mV dec^{-1})
With TENG	−0.458	2.337	128.13	2622.8
Without TENG	−0.332	0.221	95.23	1412.5

Table 3. EIS parameters for 304ss in 3.5% NaCl solution with and without the PR-TENG

		Q_{dl}		
	Rs (Ω cm^2)	Y_o (S^n Ω^{-1} cm^{-2})	n	R_{ct} (Ω cm^2)
With TENG	36.17	8.359E-6	0.7	9.957E4
Without TENG	27.6	4.801E-4	8.9	1.599E6

improved the charge transfer. At the same time, the large surface area and volume ratio of the friction layer, owing to the porous structure, not only reduced the effective thickness of the friction material, but also controlled its dielectric constant. Finally, the PR-TENG showed the maximum V_{oc} and J_{sc} of 77.1 V and 33.9 mA/m^2, respectively, which are 181.4% and 223.0% of those of the pure PDMS-based TENG under the same conditions. Furthermore, the constructed electrochemical cathodic protection system based on PR-TENG successfully converted the mechanical energy with different frequencies into electrical energy and realized the cathodic protection of the 304ss. This indicates that the PR-TENG is promising for clean energy generation and electrochemical cathodic protection.

STAR★METHODS

Detailed methods are provided in the online version of this paper and include the following:

- KEY RESOURCES TABLE
- RESOURCE AVAILABILITY
  - Lead contact
  - Materials availability
  - Data and code availability
- EXPERIMENTAL MODEL AND SUBJECT DETAILS
- METHOD DETAILS
  - Materials
  - Preparation of the negative friction layer of pure PDMS, CS/PDMS, PR/PDMS
  - Fabrication of device and cathodic protection system
  - Measurement and characterizations
- QUANTIFICATION AND STATISTICAL ANALYSIS
- ADDITIONAL RESOURCES

SUPPLEMENTAL INFORMATION

Supplemental information can be found online at https://doi.org/10.1016/j.isci.2023.108261.

ACKNOWLEDGMENTS

This work was financially supported by the National Key Research and Development Plan of China (No. 2022YFB2603000); Key R&D Program of Shandong Province, China (No. 2022CXPT027); MIITC High-tech Ship Research Projects (No. MC-202003-Z01-02); Shandong Key Laboratory of Corrosion Science, The Key Research Program of Frontier Sciences, Chinese Academy of Sciences (No. ZDBS-LY-DQC025); Wenhai Program of the S&T Fund of Shandong Province for Pilot National Laboratory for Marine Science and Technology (Qingdao) (NO. 2021WHZZB2304).

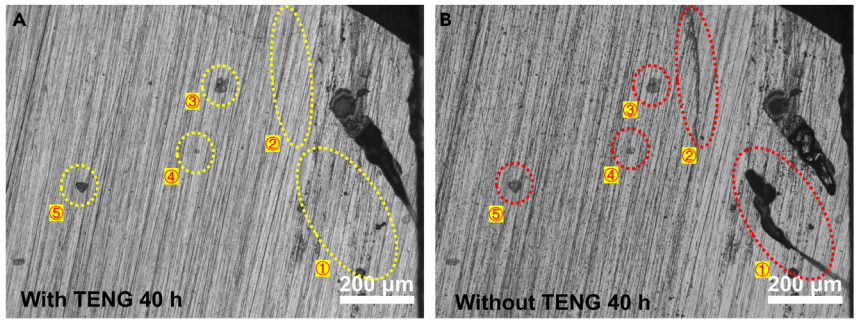

Figure 9. Optical images of 304ss
(A) with and (B) without the PR-TENG after 40 h in 3.5 wt % NaCl.

AUTHOR CONTRIBUTIONS

Y.B.N. and X.T.W. conceived the idea. Y.B.N. designed the experiments and performed data measurements. Y.B.N. and X.T.W. analyzed the data. H. Z., Y.N.S., and T. Y. helped with the experiments. Y.B.N. and X.T.W. drafted the article. X.T.W., L.H.Y, and Y.L.H. supervised this work. All authors discussed the results and commented on the article.

DECLARATION OF INTERESTS

The authors declare no competing financial interests.

Received: January 2, 2023
Revised: February 16, 2023
Accepted: October 16, 2023
Published: October 20, 2023

REFERENCES

1. Chu, S., and Majumdar, A. (2012). Opportunities and challenges for a sustainable energy future. Nature *488*, 294–303. https://doi.org/10.1038/nature11475.
2. Lin, B., and Li, Z. (2022). Towards world's low carbon development: The role of clean energy. Appl. Energy *307*, 118160. https://doi.org/10.1016/j.apenergy.2021.118160.
3. Babayomi, O.O., Dahoro, D.A., and Zhang, Z. (2022). Affordable clean energy transition in developing countries: Pathways and technologies. iScience *25*, 104178. https://doi.org/10.1016/j.isci.2022.104178.
4. Schmidt, D.G. (2016). Research Opportunities for Future Energy Technologies. ACS Energy Lett. *1*, 244–245. https://doi.org/10.1021/acsenergylett.6b00193.
5. Fan, F.-R., Tian, Z.-Q., and Lin Wang, Z. (2012). Flexible triboelectric generator. Nano Energy *1*, 328–334. https://doi.org/10.1016/j.nanoen.2012.01.004.
6. Fan, F.R., Tang, W., and Wang, Z.L. (2016). Flexible Nanogenerators for Energy Harvesting and Self-Powered Electronics. Adv. Mater. *28*, 4283–4305. https://doi.org/10.1002/adma.201504299.
7. Zhang, Q., Liang, Q., Nandakumar, D.K., Qu, H., Shi, Q., Alzakia, F.I., Tay, D.J.J., Yang, L., Zhang, X., Suresh, L., et al. (2021). Shadow enhanced self-charging power system for wave and solar energy harvesting from the ocean. Nat. Commun. *12*, 616. https://doi.org/10.1038/s41467-021-20919-9.
8. Liu, X., Mo, J., Wu, W., Song, H., and Nie, S. (2022). Triboelectric pulsed direct-current enhanced radical generation for efficient degradation of organic pollutants in wastewater. Appl. Catal. B Environ. *312*, 121422. https://doi.org/10.1016/j.apcatb.2022.121422.
9. Shao, Z., Chen, J., Gao, K., Xie, Q., Xue, X., Zhou, S., Huang, C., Mi, L., and Hou, H. (2022). A Double-Helix Metal-Chain Metal-Organic Framework as a High-Output Triboelectric Nanogenerator Material for Self-Powered Anticorrosion. Angew. Chem. Int. Ed. Engl. *61*, e202208994. https://doi.org/10.1002/anie.202208994.
10. Zhu, H.R., Tang, W., Gao, C.Z., Han, Y., Li, T., Cao, X., and Wang, Z.L. (2015). Self-powered metal surface anti-corrosion protection using energy harvested from rain drops and wind. Nano Energy *14*, 193–200. https://doi.org/10.1016/j.nanoen.2014.11.041.
11. Zhou, L., Liu, D., Li, S., Yin, X., Zhang, C., Li, X., Zhang, C., Zhang, W., Cao, X., Wang, J., and Wang, Z.L. (2019). Effective removing of hexavalent chromium from wasted water by triboelectric nanogenerator driven self-powered electrochemical system – Why pulsed DC is better than continuous DC? Nano Energy *64*, 103915. https://doi.org/10.1016/j.nanoen.2019.103915.
12. Leung, S.-F., Fu, H.-C., Zhang, M., Hassan, A.H., Jiang, T., Salama, K.N., Wang, Z.L., and He, J.-H. (2020). Blue energy fuels: converting ocean wave energy to carbon-based liquid fuels via CO2 reduction. Energy Environ. Sci. *13*, 1300–1308. https://doi.org/10.1039/c9ee03566d.
13. Xu, C., Liu, Y., Liu, Y., Zheng, Y., Feng, Y., Wang, B., Kong, X., Zhang, X., and Wang, D. (2020). New inorganic coating-based triboelectric nanogenerators with anti-wear and self-healing properties for efficient wave energy harvesting. Appl. Mater. Today *20*, 100645. https://doi.org/10.1016/j.apmt.2020.100645.
14. Liu, X., Xu, X., Zhang, F., Ge, X., Ji, H., Li, Y., Lu, S., and Wen, Z. (2022). A synergistic anti-corrosion system based on durable superhydrophobic F-SiO2/epoxy coatings and self-powered cathodic protection. J. Mater. Chem. A Mater. *10*, 18616–18625. https://doi.org/10.1039/D2TA05071D.
15. Yang, Y., Zhang, H., Chen, J., Jing, Q., Zhou, Y.S., Wen, X., and Wang, Z.L. (2013). Single-Electrode-Based Sliding Triboelectric Nanogenerator for Self-Powered Displacement Vector Sensor System. ACS Nano *7*, 7342–7351. https://doi.org/10.1021/nn403021m.
16. Jiang, T., Chen, X., Han, C.B., Tang, W., and Wang, Z.L. (2015). Theoretical Study of Rotary Freestanding Triboelectric Nanogenerators. Adv. Funct. Mater. *25*, 2928–2938. https://doi.org/10.1002/adfm.201500447.
17. Zhao, P., Soin, N., Prashanthi, K., Chen, J., Dong, S., Zhou, E., Zhu, Z., Narasimulu, A.A., Montemagno, C.D., Yu, L., and Luo, J. (2018). Emulsion Electrospinning of Polytetrafluoroethylene (PTFE) Nanofibrous Membranes for High-Performance Triboelectric Nanogenerators. ACS Appl. Mater. Interfaces *10*, 5880–5891. https://doi.org/10.1021/acsami.7b18442.
18. Wang, H.L., Guo, Z.H., Zhu, G., Pu, X., and Wang, Z.L. (2021). Boosting the Power and Lowering the Impedance of Triboelectric Nanogenerators through Manipulating the Permittivity for Wearable Energy Harvesting. ACS Nano *15*, 7513–7521. https://doi.org/10.1021/acsnano.1c00914.
19. Seol, M., Kim, S., Cho, Y., Byun, K.E., Kim, H., Kim, J., Kim, S.K., Kim, S.W., Shin, H.J., and Park, S. (2018). Triboelectric Series of 2D Layered Materials. Adv. Mater. *30*, e1801210. https://doi.org/10.1002/adma.201801210.
20. Cai, C., Luo, B., Liu, Y., Fu, Q., Liu, T., Wang, S., and Nie, S. (2022). Advanced triboelectric materials for liquid energy harvesting and emerging application. Mater. Today *52*, 299–326. https://doi.org/10.1016/j.mattod.2021.10.034.
21. Khandelwal, G., Maria Joseph Raj, N.P., and Kim, S.J. (2021). Materials Beyond Conventional Triboelectric Series for Fabrication and Applications of Triboelectric Nanogenerators. Adv. Energy Mater. *11*, 2101170. https://doi.org/10.1002/aenm.202101170.
22. Hajra, S., Panda, J., Swain, J., Kim, H.-G., Sahu, M., Rana, M.K., Samantaray, R., Kim, H.J., and Sahu, R. (2022). Triazine skeletal covalent organic frameworks: A versatile highly positive surface potential triboelectric layer for energy harvesting and self-powered applications. Nano Energy *101*, 107620. https://doi.org/10.1016/j.nanoen.2022.107620.
23. Kim, D., Park, S.-J., Jeon, S.-B., Seol, M.-L., and Choi, Y.-K. (2016). A Triboelectric Sponge Fabricated from a Cube Sugar Template by 3D Soft Lithography for Superhydrophobicity and Elasticity. Adv. Electron. Mater. *2*, 1500331. https://doi.org/10.1002/aelm.201500331.
24. Chakraborty, I., Lai, S.N., Wu, M.C., Lin, H.Y., Li, C., Wu, J.M., and Lai, C.S. (2021). Charge trapping with alpha-Fe2O3 nanoparticles accompanied by human hair towards an enriched triboelectric series and a sustainable circular bioeconomy. Mater. Horiz. *8*, 3149–3162. https://doi.org/10.1039/d1mh00919b.
25. Harnchana, V., Ngoc, H.V., He, W., Rasheed, A., Park, H., Amornkitbamrung, V., and Kang, D.J. (2018). Enhanced Power Output of a Triboelectric Nanogenerator using Poly(dimethylsiloxane) Modified with Graphene Oxide and Sodium Dodecyl Sulfate. ACS Appl. Mater. Interfaces *10*,

25263–25272. https://doi.org/10.1021/acsami.8b02495.

26. Ni, G.-L., Zhu, X., Mi, H.-Y., Feng, P.-Y., Li, J., Jing, X., Dong, B., Liu, C., and Shen, C. (2021). Skinless porous films generated by supercritical CO2 foaming for high-performance complementary shaped triboelectric nanogenerators and self-powered sensors. Nano Energy *87*, 106148. https://doi.org/10.1016/j.nanoen.2021.106148.
27. Barras, R., dos Santos, A., Calmeiro, T., Fortunato, E., Martins, R., Águas, H., Barquinha, P., Igreja, R., and Pereira, L. (2021). Porous PDMS conformable coating for high power output carbon fibers/ZnO nanorod-based triboelectric energy harvesters. Nano Energy *90*, 106582. https://doi.org/10.1016/j.nanoen.2021.106582.
28. Jang, S., and Oh, J.H. (2018). Rapid Fabrication of Microporous BaTiO3/PDMS Nanocomposites for Triboelectric Nanogenerators through One-step Microwave Irradiation. Sci. Rep. *8*, 14287. https://doi.org/10.1038/s41598-018-32609-6.
29. Fan, B., Liu, G., Fu, X., Wang, Z., Zhang, Z., and Zhang, C. (2022). Composite film with hollow hierarchical silica/perfluoropolyether filler and surface etching for performance enhanced triboelectric nanogenerators. Chem. Eng. J. *446*, 137263. https://doi.org/10.1016/j.cej.2022.137263.
30. Chen, J., Guo, H., He, X., Liu, G., Xi, Y., Shi, H., and Hu, C. (2016). Enhancing Performance of Triboelectric Nanogenerator by Filling High Dielectric Nanoparticles into Sponge PDMS Film. ACS Appl. Mater. Interfaces *8*, 736–744. https://doi.org/10.1021/acsami.5b09907.
31. Hazarika, A., Deka, B.K., Kim, D.C., Jaiswal, A.P., Seo, J., Park, Y.-B., Kim, J., and Park, H.W. (2022). Multidimensional wearable self-powered personal thermal management with scalable solar heating and a triboelectric nanogenerator. Nano Energy *98*, 107323. https://doi.org/10.1016/j.nanoen.2022.107323.
32. Sahu, M., Vivekananthan, V., Hajra, S., Khatua, D.K., and Kim, S.-J. (2021). Porosity modulated piezo-triboelectric hybridized nanogenerator for sensing small energy impacts. Appl. Mater. Today *22*, 100900. https://doi.org/10.1016/j.apmt.2020.100900.
33. Seo, J., Hajra, S., Sahu, M., and Kim, H.J. (2021). Effect of cilia microstructure and ion injection upon single-electrode triboelectric nanogenerator for effective energy harvesting. Mater. Lett. *304*, 130674. https://doi.org/10.1016/j.matlet.2021.130674.
34. Li, Y., Liu, Y., Ren, Y., Su, L., Li, A., An, Y., Rotello, V., Zhang, Z., Wang, Y., Liu, Y., et al. (2020). Enhancement of Triboelectric Charge Density by Chemical Functionalization. Adv. Funct. Mater. *30*, 2004942. https://doi.org/10.1002/adfm.202004714.
35. Xia, S.-Y., Long, Y., Huang, Z., Zi, Y., Tao, L.-Q., Li, C.-H., Sun, H., and Li, J. (2022). Laser-induced graphene (LIG)-based pressure sensor and triboelectric nanogenerator towards high-performance self-powered measurement-control combined system. Nano Energy *96*, 107099. https://doi.org/10.1016/j.nanoen.2022.107099.
36. Zhang, W., Lu, Y., Liu, T., Zhao, J., Liu, Y., Fu, Q., Mo, J., Cai, C., and Nie, S. (2022). Spheres Multiple Physical Network-Based Triboelectric Materials for Self-Powered Contactless Sensing. Small *18*, e2200577. https://doi.org/10.1002/smll.202200577.
37. Sun, X., Liu, Y., Luo, N., Liu, Y., Feng, Y., Chen, S., and Wang, D. (2022). Controlling the triboelectric properties and tribological behavior of polyimide materials via plasma treatment. Nano Energy *102*, 107691. https://doi.org/10.1016/j.nanoen.2022.107691.
38. Lee, B.-Y., Kim, S.-U., Kang, S., and Lee, S.-D. (2018). Transparent and flexible high power triboelectric nanogenerator with metallic nanowire-embedded tribonegative conducting polymer. Nano Energy *53*, 152–159. https://doi.org/10.1016/j.nanoen.2018.08.048.
39. Sriphan, S., and Vittayakorn, N. (2018). Facile roughness fabrications and their roughness effects on electrical outputs of the triboelectric nanogenerator. Smart Mater. Struct. *27*, 105026. https://doi.org/10.1088/1361-665X/aadb65.
40. Sun, Y., Zheng, Y., Wang, R., Lei, T., Liu, J., Fan, J., Shou, W., and Liu, Y. (2022). 3D micro-nanostructure based waterproof triboelectric nanogenerator as an outdoor adventure power source. Nano Energy *100*, 107506. https://doi.org/10.1016/j.nanoen.2022.107506.
41. Wang, S., Lin, L., and Wang, Z.L. (2012). Nanoscale triboelectric-effect-enabled energy conversion for sustainably powering portable electronics. Nano Lett. *12*, 6339–6346. https://doi.org/10.1021/nl303573d.
42. Huang, J., Li, Z., Liang, W., Chen, B., Hu, J., Yang, W., and Jiang, L. (2019). Micro/nano-structures-enhanced triboelectric nanogenerators by femtosecond laser direct writing. Nano Energy *59*, 638–645. https://doi.org/10.1016/j.nanoen.2019.05.081.
43. Li, S., Fan, Y., Chen, H., Nie, J., Liang, Y., Tao, X., Zhang, J., Chen, X., Fu, E., and Wang, Z.L. (2020). Manipulating the triboelectric surface charge density of polymers by low-energy helium ion irradiation/implantation. Energy Environ. Sci. *13*, 896–907. https://doi.org/10.1039/c9ee03307f.
44. Jiang, C., Li, X., Yao, Y., Lan, L., Shao, Y., Zhao, F., Ying, Y., and Ping, J. (2019). A multifunctional and highly flexible triboelectric nanogenerator based on MXene-enabled porous film integrated with laser-induced graphene electrode. Nano Energy *66*, 104121. https://doi.org/10.1016/j.nanoen.2019.104121.
45. Fan, Y.J., Meng, X.S., Li, H.Y., Kuang, S.Y., Zhang, L., Wu, Y., Wang, Z.L., and Zhu, G. (2017). Stretchable Porous Carbon Nanotube-Elastomer Hybrid Nanocomposite for Harvesting Mechanical Energy. Adv. Mater. *29*, 1603115. https://doi.org/10.1002/adma.201603115.
46. Cui, C., Wang, X., Yi, Z., Yang, B., Wang, X., Chen, X., Liu, J., and Yang, C. (2018). Flexible Single-Electrode Triboelectric Nanogenerator and Body Moving Sensor Based on Porous Na2CO3/Polydimethylsiloxane Film. ACS Appl. Mater. Interfaces *10*, 3652–3659. https://doi.org/10.1021/acsami.7b17585.
47. Nikpour, S., Ansari-Asl, Z., Sedaghat, T., and Hoveizi, E. (2022). Curcumin-loaded Fe-MOF/PDMS porous scaffold: Fabrication, characterization, and biocompatibility assessment. J. Ind. Eng. Chem. *110*, 188–197. https://doi.org/10.1016/j.jiec.2022.02.052.
48. Lancastre, J.J.H., Fernandes, N., Margaça, F., Miranda Salvado, I.M., Ferreira, L.M., Falcão, A., and Casimiro, M.H. (2012). Study of PDMS conformation in PDMS-based hybrid materials prepared by gamma irradiation. Radiat. Phys. Chem. *81*, 1336–1340. https://doi.org/10.1016/j.radphyschem.2012.02.016.
49. Cao, R., Zhang, X., Wu, H., Wang, J., Liu, X., and Jiang, Z. (2011). Enhanced pervaporative desulfurization by polydimethylsiloxane membranes embedded with silver/silica core-shell microspheres. J. Hazard Mater. *187*, 324–332. https://doi.org/10.1016/j.jhazmat.2011.01.031.
50. Lee, K.Y., Chun, J., Lee, J.H., Kim, K.N., Kang, N.R., Kim, J.Y., Kim, M.H., Shin, K.S., Gupta, M.K., Baik, J.M., and Kim, S.W. (2014). Hydrophobic sponge structure-based triboelectric nanogenerator. Adv. Mater. *26*, 5037–5042. https://doi.org/10.1002/adma.201401184.
51. He, X., Mu, X., Wen, Q., Wen, Z., Yang, J., Hu, C., and Shi, H. (2016). Flexible and transparent triboelectric nanogenerator based on high performance well-ordered porous PDMS dielectric film. Nano Res. *9*, 3714–3724. https://doi.org/10.1007/s12274-016-1242-3.
52. Zheng, Q., Fang, L., Guo, H., Yang, K., Cai, Z., Meador, M.A.B., and Gong, S. (2018). Highly Porous Polymer Aerogel Film-Based Triboelectric Nanogenerators. Adv. Funct. Mater. *28*, 1706365. https://doi.org/10.1002/adfm.201706365.
53. Zhu, G., Lin, Z.H., Jing, Q., Bai, P., Pan, C., Yang, Y., Zhou, Y., and Wang, Z.L. (2013). Toward large-scale energy harvesting by a nanoparticle-enhanced triboelectric nanogenerator. Nano Lett. *13*, 847–853. https://doi.org/10.1021/nl4001053.
54. Wang, J., Wu, C., Dai, Y., Zhao, Z., Wang, A., Zhang, T., and Wang, Z.L. (2017). Achieving ultrahigh triboelectric charge density for efficient energy harvesting. Nat. Commun. *8*, 88. https://doi.org/10.1038/s41467-017-00131-4.
55. Cheng, L., Xu, Q., Zheng, Y., Jia, X., and Qin, Y. (2018). A self-improving triboelectric nanogenerator with improved charge density and increased charge accumulation speed. Nat. Commun. *9*, 3773. https://doi.org/10.1038/s41467-018-06045-z.
56. Liu, S., Zheng, W., Yang, B., and Tao, X. (2018). Triboelectric charge density of porous and deformable fabrics made from polymer fibers. Nano Energy *53*, 383–390. https://doi.org/10.1016/j.nanoen.2018.08.071.
57. Ding, P., Chen, J., Farooq, U., Zhao, P., Soin, N., Yu, L., Jin, H., Wang, X., Dong, S., and Luo, J. (2018). Realizing the potential of polyethylene oxide as new positive tribo-material: Over 40 W/m2 high power flat surface triboelectric nanogenerators. Nano Energy *46*, 63–72. https://doi.org/10.1016/j.nanoen.2018.01.034.
58. Oh, W., Hajra, S., Divya, S., Panda, S., Oh, Y., Jaglic, Z., Pakawanit, P., Oh, T.H., and Kim, H.J. (2023). Contact electrification of porous PDMS-nickel ferrite composites for effective energy harvesting. Mater. Sci. Eng., B *292*, 116397. https://doi.org/10.1016/j.mseb.2023.116397.
59. Yang, W., Liu, Y., Zhang, Z., Li, Q., Yu, T., and Li, Y. (2023). Scalable, flexible, and

hierarchical porous conductive nanocomposites for self-powered and pressure sensing dual-mode integration. Compos. Sci. Technol. *232*, 109884. https://doi.org/10.1016/j.compscitech.2022.109884.

60. Xie, Y., Hu, J., Li, H., Mi, H.-Y., Ni, G., Zhu, X., Jing, X., Wang, Y., Zheng, G., Liu, C., and Shen, C. (2022). Green fabrication of double-sided self-supporting triboelectric nanogenerator with high durability for energy harvesting and self-powered sensing. Nano Energy *93*, 106827. https://doi.org/10.1016/j.nanoen.2021.106827.
61. Li, Z., Hu, K., Yang, M., Zou, Y., Yang, J., Yu, M., Wang, H., Qu, X., Tan, P., Wang, C., et al. (2019). Elastic Cu@PPy sponge for hybrid device with energy conversion and storage. Nano Energy *58*, 852–861. https://doi.org/10.1016/j.nanoen.2018.11.093.
62. Shao, Y., Luo, C., Deng, B.-W., Yin, B., and Yang, M.-B. (2020). Flexible porous silicone rubber-nanofiber nanocomposites generated by supercritical carbon dioxide foaming for harvesting mechanical energy. Nano Energy *67*, 104290. https://doi.org/10.1016/j.nanoen.2019.104290.

STAR★METHODS

KEY RESOURCES TABLE

REAGENT or RESOURCE	SOURCE	IDENTIFIER
Chemicals, peptides, and recombinant proteins		
Chitosan	Shanghai Chemical Reagent Co., LTD	Cat# 69047434; CAS: 9012-76-4
Sylgard 184	Dow Corning	www.dow.com/zh-cn/pdp.sylgard-184-silicone-elastomer-kit.01064291z.html#overview
Anodic Aluminum Oxide (AAO)	Hefei Jinghui Nano Technology Co., LTD	www.pynano66.com
Kapton tape	Shenzhen New Hongsen Technology Co., LTD	www.11467.com/shenzhen/co/1137344.htm
Double-sided foam tape and copper tape	3 M Shanghai Duzhen Industrial Co., LTD	www.3m.com.cn/3M/zh_CN/p/c/tapes/

RESOURCE AVAILABILITY

Lead contact

Further information and requests for resources and reagents should be directed to and will be fulfilled by the lead contact, Xiutong Wang (wangxiutong@qdio.ac.cn).

Materials availability

This work is an experimental study of triboelectric nanogenerators and its application for electrochemical cathodic protection and there is no new code generated.

Data and code availability

All data reported in this paper will be shared by the lead contact upon reasonable request.
No new code was generated during the course of this study.
Any additional information required to reanalyze the data reported in this paper is available from the lead contact upon reasonable request.

EXPERIMENTAL MODEL AND SUBJECT DETAILS

This study does not use experimental methods typical in the life sciences.

METHOD DETAILS

Materials

Chitosan was purchased from Shanghai Chemical Reagent Co., LTD. Sylgard 184 was purchased from Dow Corning. Anodic Aluminum Oxide (AAO) was purchased from Hefei Jinghui Nano Technology Co., LTD. The acrylic sheet was purchased from a local market. The Kapton tape was obtained from Shenzhen New Hongsen Technology Co., LTD. The double-sided foam tape and copper tape were obtained from 3 M Shanghai Duzhen Industrial Co., LTD.

Preparation of the negative friction layer of pure PDMS, CS/PDMS, PR/PDMS

Sylgard 184 part A (2 g) and part B (0.2 g), ratio of 10:1, were weighted, slowly transferred to a beaker with a syringe, and stired to obtain a uniform PDMS viscous solution. Chitosan (0.5 g) with a molecular weight of 50,000 was placed in a centrifuge tube filled with ethanol (10 mL) and ultrasonicated to obtain a uniform suspension. The obtained suspension was then poured into the PDMS viscous solution and stirred well. A square mold was formed by adhering Kapton tape (thickness of 0.118 mm) around the 10 × 10 cm acrylic sheet. The PDMS viscous solution containing chitosan was slowly inverted on the square mold and allowed to stand for 5 min to ensure even distribution in the template. Next, the AAO (pore size: 100 nm or 300 nm) template was paced on the viscous liquid and let to stand for 5 min. Subsequently, the liquid with the template was vacuum-dried at 60°C for 2 h. After cooling to room temperature, the film was peeled off from the template, and the AAO template was dissolved with 0.2 M NaOH to obtain PR/PDMS. PR/PDMS prepared with 100 nm and 300 nm AAO were PR/ PDMS-0.54 and PR/ PDMS-1.7, respectively. Pure PDMS and CS/PDMS were obtained following the same procedure, but without the addition of chitosan and application of the AAO template, respectively.

Fabrication of device and cathodic protection system

Springs were used as supporting points to assemble different electrodes in sandwich-like TENGs. First, 15×15 mm double-sided foam tape and copper tape were sequentially fixed at the center of the 40×40 mm acrylic board using double-sided tape. Next, the negative friction layer (pure PDMS, CS/PDMS, or PR/PDMS) was fixed on the copper tape and connected to a 15 cm copper wire. A 15×15 mm piece of aluminum foil was fixed at the center of another acrylic sheet with a size of 40×40 mm and connected to a 15 cm copper wire. Finally, the above two acrylic sheets were assembled using 4 spring connections to obtain a sandwich-like TENG with vertical contact separation.

The electrochemical cathodic protection system was assembled by rectifying the TENG full-bridge and connecting it to a three-electrode electrolysis cell. The counter electrode (CE) Pt was connected to the positive electrode; 304ss was the working electrode (WE) connected to the negative electrode; the reference electrode (RE) was saturated calomel electrode (SCE); 3.5% NaCl was used as the electrolyte to simulate seawater. If not specified otherwise, the above characterization was used PR-TENG based on PR/PDMS-1.7.

Measurement and characterizations

The morphologies of the negative friction layers were characterized using scanning electron microscopy (SEM, HITACHI Regulus 8100, Japan) and laser scanning confocal microscopy (LSCM, LEXT OLS5000, Japan). The composition of the samples was explored using X-ray diffraction (XRD, Bruker D8ADVANCE, Germany). FTIR (NicoletiS50, Thermo Fisher, USA) was conducted to analyze the molecular structure of samples. The performance of the TENGs was evaluated using a shaker with signal generator (JZK-5, SINOCERA PIEZOTRONIC, Jiangsu, China). The V_{oc} and J_{sc} of TENG were measured using a Keithley 6517B electrometer (Keithley6514, Tectronix, China). The cathodic protection parameters were evaluated using an electrochemical workstation (CHI760E, Shanghai Chen Hua, China).

QUANTIFICATION AND STATISTICAL ANALYSIS

The TENG data were collected with a Keithley 6514 system electrometer. Figures were produced by Origin from the raw data.

ADDITIONAL RESOURCES

This study has not generated or contributed to a new website/forum.